9th International Conference on Fracture Mechanics of Concrete and Concrete Structures
FraMCoS-9
V. Saouma, J. Bolander, and E. Landis (Eds)

DOI 10.21012/FC9.172

# LATTICE DISCRETE PARTICLE MODELING (LDPM) OF FLEXURAL SIZE EFFECT IN OVER REINFORCED CONCRETE BEAMS

**MOHAMMED ALNAGGAR***, **DANIELE PELESSONE**[†] **AND GIANLUCA CUSATIS**[‡]

*Rensselaer Polytechnic Institute
Troy, NY USA
e-mail: alnagm2@rpi.edu

[†]ES3 Inc.
San Diego, CA USA
e-mail: daniele.pelessone@es3inc.com

[‡]Northwestern University
Evanston, IL USA
e-mail: g-cusatis@northwestern.edu

**Key words:** Reinforcend Concrete, Size Effect, Lattice Discrete Particle Model

**Abstract.** At the macroscopic scale, concrete can be approximated as statistically homogeneous. Nevertheless, its macroscopic behavior shows quasi-brittleness, strain softening, and size effects evidencing a strong influence of material heterogeneity. A model naturally accounting for material heterogeneity is the Lattice Discrete Particle Model (LDPM). LDPM replaces the actual concrete mesostructure by an assemblage of discrete particles interacting through nonlinear and fracturing lattice struts. Each particle represents one coarse aggregate piece. Since the initial development, LDPM has shown superior material modeling capabilities. In this research, LDPM is used to simulate the flexural failure of three groups of over reinforced concrete beams. The groups represent 1D, 2D and 3D geometric similarities. Geometry is generated based on concrete mix design. Then calibration was only guided by the experimentally provided compressive strength. In order to reduce the redundancy of the calibration process, the fracture properties of concrete were estimated using relevant literature. Finally, the rebar assembly was connected to the LDPM mesh using penalty type constraints and the rebars were modeled using 1D beam elements. Numerical results show excellent agreement with experimental data and clear capability of capturing size effects.

## 1 INTRODUCTION

There is no doubt that we live in the high rise buildings era. Every day, higher altitudes are sought. From the +850 m Burj Khalifa in Dubai, UAE, to the next world record coming +1000 m Kingdom Tower in Saudi Arabia, we have built structures so high. Interestingly, these structures are not steel dominated as the past century trends. Thanks to the concrete manufacturing and construction technologies, concrete was pumped to +600 m in Burj Khalifa. In addition, the world urbanization has put even more demand on such type of buildings, calling for the Mega Cities type of high rise buildings. For such structures to withstand the mighty forces of both earthquakes and wind loads, they ought to have lateral supporting systems that consist of heavily reinforced members with reinforcements in both sides. This demand leads in many cases to the violation of the preferable under-reinforced design consideration. With concrete being overstressed in compression and bending, a well experimentally known behavior is brought to consideration which is the size effect (See for example the research by [1–4]), which shows that the structural member strength reduces with the increase of its size for a multitude of different tests. The explanation of this phenomenon can be related to statistical size effect [5], energetic size effect [6], or both. The material strength randomness as described by statistical distributions like the Weibull distribution explains the statistical type while, for the energetic one, the reason is that the rate of energy release into an advancing crack tip scales with structure size, while the ability of a unit area of that advancing crack tip to dissipate energy is approximately independent of the structure size.

Specifically for over-reinforced beams, a limited effort was pursued. Earlier studies have analyzed over-reinforced concrete beams with limited size change and fracture [7, 8]. A larger size range with one, two and three dimensional similarities was introduced by [3]. Additional work on concrete size effect in compression has been pursued by several researchers [9–11] that showed different degrees of size effect.

From a modeling point of view, the main challenge in capturing size effect in compression is related to the multiple cracking that takes place in the over stressed concrete zone before failure. The lattice Discrete Particle Model (LDPM) [12] used in this study, can replicate this realistically by reproducing internal aggregate to aggregate strut and tie behavior while almost all continuum based formulations represent compressive damage by fictitious compression softening. LDPM not only successfully captures such complicated cracking, it also replicates the different theoretical stages of concrete failure and shows realistic modes of failure both quantitatively and qualitatively.

## 2 MODELING OF RC BEAMS

To correctly capture size effect while replicating realistic cracking in the post peak, the Lattice Discrete Particle Model (LDPM) has been utilized to represent concrete behavior. As the beams under consideration were all over reinforced, the rebar model used was elastic-perfectly plastic. Finally, the bond between rebars and concrete was assumed to be perfect and thus, a penalty algorithm has been used to connect the rebar nodes to the concrete nodes. The following subsections describe each of the material mechanical models used.

### 2.1 The Lattice Discrete Particle Model (LDPM)

The Lattice Discrete Particle Model (LDPM) [12, 13] is a meso-scale discrete model that simulates the mechanical interaction of coarse aggregate pieces embedded in a cementitious matrix (mortar). The geometrical representation of concrete mesostructure is constructed through the following steps. 1) The coarse aggregate pieces, whose shapes are assumed to be spherical, are introduced into the concrete volume by a try-and-reject random procedure. 2) Zero-radius aggregate pieces (nodes) are randomly distributed over the external surfaces to facilitate the application of boundary conditions. 3) A three-dimensional domain tessellation, based on the Delaunay tetrahedralization of the generated aggregate centers, creates a system of polyhedral cells (see Fig. 1) interacting through triangular facets and a lattice system composed by the line segments connecting the particle centers.

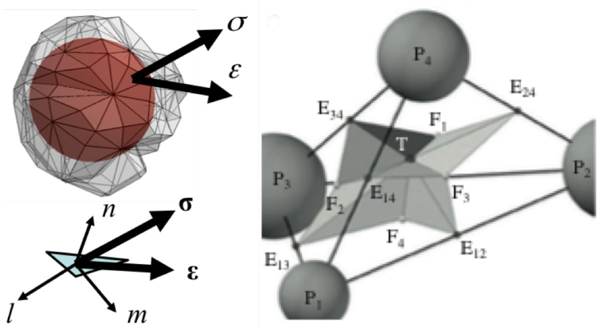


Figure 1: LDPM polyhedral cell, facet vectorial stresses and strains and the lattice system

In LDPM, rigid body kinematics is used to describe the deformation of the lattice/particle system and the displacement jump, $[\![\mathbf{u}_C]\!]$, at the centroid of each facet is used to define measures of strain as

$$e_N = \frac{\mathbf{n}^{\mathrm{T}}[\![\mathbf{u}_C]\!]}{\ell}; \quad e_L = \frac{\mathbf{l}^{\mathrm{T}}[\![\mathbf{u}_C]\!]}{\ell}; \quad e_M = \frac{\mathbf{m}^{\mathrm{T}}[\![\mathbf{u}_C]\!]}{\ell} \tag{1}$$

where $\ell$ = interparticle distance; and $\mathbf{n}$, $\mathbf{l}$, and $\mathbf{m}$, are unit vectors defining a local system of reference attached to each facet. It was recently demonstrated that the strain definitions in Eq. 1 correspond to the projection into the local system of references of the strain tensor typical of continuum mechanics [14–16]

Next, a vectorial constitutive law governing the behavior of the material is imposed at the centroid of each facet. In the elastic regime, the normal and shear stresses are proportional to the corresponding strains: $t_N = E_N e_N^* = E_N(e_N - e_N^0)$; $t_M = E_T e_M^* = E_T(e_M - e_M^0)$; $t_L = E_T e_L^* = E_T(e_L - e_L^0)$, where $E_N = E_0$, $E_T = \alpha E_0$, $E_0$ = effective normal modulus, and $\alpha$ = shear-normal coupling parameter; and $e_N^0$, $e_M^0$, $e_L^0$ are mesoscale eigenstrains that might arise from a variety of phenomena such as, but not limited to, thermal expansion, shrinkage, and ASR expansion.

For stresses and strains beyond the elastic limit, LDPM mesoscale nonlinear phenomena are characterized by three mechanisms as described below.

**Fracture and cohesion due to tension and tension-shear.** For tensile loading ($e_N^* > 0$), the fracturing behavior is formulated through an effective strain, $e = \sqrt{e_N^{*2} + \alpha(e_M^{*2} + e_L^{*2})}$, and stress, $t = \sqrt{t_N^2 + (t_M + t_L)^2/\alpha}$, which define the normal and shear stresses as $t_N = e_N^*(t/e)$; $t_M = \alpha e_M^*(t/e)$; $t_L = \alpha e_L^*(t/e)$. The effective stress $t$ is incrementally elastic ($\dot{t} = E_0 \dot{e}$) and must satisfy the inequality $0 \leq t \leq \sigma_{bt}(e,\omega)$ where $\sigma_{bt} = \sigma_0(\omega)\exp\left[-H_0(\omega)\langle e - e_0(\omega)\rangle/\sigma_0(\omega)\right]$, $\langle x \rangle = \max\{x, 0\}$, and $\tan(\omega) = e_N^*/\sqrt{\alpha}e_T^* = t_N\sqrt{\alpha}/t_T$, and $e_T^* = \sqrt{e_M^{*2} + e_L^{*2}}$. The post peak softening modulus is defined as $H_0(\omega) = H_t(2\omega/\pi)^{n_t}$, where $H_t$ is the softening modulus in pure tension ($\omega = \pi/2$) expressed as $H_t = 2E_0/\left(l_t/l_e - 1\right)$; $l_t = 2E_0 G_t/\sigma_t^2$; $l_e$ is the length of the tetrahedron edge; and $G_t$ is the mesoscale fracture energy. LDPM provides a smooth transition between pure tension and pure shear ($\omega = 0$) with parabolic variation for strength given by $\sigma_0(\omega) = \sigma_t r_{st}^2 \Big( -\sin(\omega) + \sqrt{\sin^2(\omega) + 4\alpha\cos^2(\omega)/r_{st}^2}\Big) \,/\, [2\alpha\cos^2(\omega)]$, where $r_{st} = \sigma_s/\sigma_t$ is the ratio of shear strength to tensile strength.

**Compaction and pore collapse from compression.** Normal stresses for compressive loading ($e_N^* < 0$) are computed through the inequality $-\sigma_{bc}(e_D, e_V) \leq t_N \leq 0$, where $\sigma_{bc}$ is a strain-dependent boundary function of the volumetric strain, $e_V$, and the deviatoric strain, $e_D = e_N - e_V$. The volumetric strain is computed by the volume variation of the Delaunay tetrahedra as $e_V = \Delta V/3V_0$ and is assumed to be constant for all facets belonging to a given tetrahedron. Beyond the elastic limit, $-\sigma_{bc}$ models pore collapse as a linear evolution of stress for increasing volumetric strain with stiffness $H_c$ for $-e_V \leq e_{c1} = \kappa_{c0}e_{c0}$: $\sigma_{bc} = \sigma_{c0} + \langle -e_V - e_{c0}\rangle H_c(r_{DV})$; $H_c(r_{DV}) = H_{c0}/(1 + \kappa_{c2}\langle r_{DV} - \kappa_{c1}\rangle)$; $\sigma_{c0}$ is the mesoscale compressive yield stress; $r_{DV} = e_D/e_V$ and $\kappa_{c1}$, $\kappa_{c2}$ are material parameters. Compaction and rehardening occur beyond pore collapse ($-e_V \geq e_{c1}$). In this case one has $\sigma_{bc} = \sigma_{c1}(r_{DV})\,\exp\left[(-e_V - e_{c1})H_c(r_{DV})/\sigma_{c1}(r_{DV})\right]$ and $\sigma_{c1}(r_{DV}) = \sigma_{c0} + (e_{c1} - e_{c0})H_c(r_{DV})$.

**Friction due to compression-shear.** The incremental shear stresses are computed as $\dot{t}_M = E_T(\dot{e}_M^* - \dot{e}_M^{*p})$ and $\dot{t}_L = E_T(\dot{e}_L^* - \dot{e}_L^{*p})$, where $\dot{e}_M^{*p} = \dot{\lambda}\partial\varphi/\partial t_M$, $\dot{e}_L^{*p} = \dot{\lambda}\partial\varphi/\partial t_L$, and $\lambda$ is the plastic multiplier with loading-unloading conditions $\varphi\dot{\lambda} \leq 0$ and $\dot{\lambda} \geq 0$. The plastic potential is defined as $\varphi = \sqrt{t_M^2 + t_L^2} - \sigma_{bs}(t_N)$, where the nonlinear frictional law for the shear strength is assumed to be $\sigma_{bs} = \sigma_s + (\mu_0 - \mu_\infty)\sigma_{N0}[1 - \exp(t_N/\sigma_{N0})] - \mu_\infty t_N$; $\sigma_{N0}$ is the transitional normal stress; $\mu_0$ and $\mu_\infty$ are the initial and final internal friction coefficients.

Finally, the governing equations of the LDPM framework are completed through the equilibrium equations of each individual particle.

LDPM has been used successfully to simulate concrete behavior under a large variety of loading conditions [12, 13]. Furthermore it can be properly formulated to account for fiber reinforcement [17, 18] and it was recently extended to simulate the ballistic behavior of ultra-high performance concrete (UHPC) [19]. In addition, LDPM was successfully used in structural element scale analysis using multiscale methods [20–22].

### 2.2 Rebar Concrete interaction Model

The model presented here represents concrete using the Lattice Discrete Particle Model (LDPM) and steel rebars using 1D beam finite elements. First, a review of the kinematic assumptions on the motion of concrete and steel reinforcement is presented, then, kinematic conditions are imposed to constrain their relative motion and interactive forces between the two are derived.

### 2.3 Kinematic description

Consider a body made of concrete material occupying a volume $V$ in a three dimensional space. Each point inside the volume $V$ can be identified by its cartesian coordinates $\mathbf{x}$. The motion of point $\mathbf{x}$ can be described by velocity and displacement time histories, respectively $\mathbf{v}(\mathbf{x}, t)$ and $\mathbf{u}(\mathbf{x}, \mathbf{t})$, where $t$ is the time parameter. In the LDPM framework, the motion of all material points inside $V$ can be described in two different ways. On one hand, one can relate the motion of a material point to the deformations of the tetrahedral LDPM elements that contains it. At time 0, these tetrahedral elements fill the entire volume $V$ and each material point is either inside an element or may be shared with other elements if it is on a tetrahedral surface. Tetrahedral elements deform linearly according to the motion of the vertex particles. Thus, the motion of a material point $\mathbf{x}$ can be described by the relationship

$$\mathbf{u}(\mathbf{x}, t) = \sum_{i=1}^{4} N_i(\xi)\, \mathbf{u_i}(t) \tag{2}$$

where $\mathbf{u_i}(t)$ are the displacement histories of the four vertex particles defining the element that contains point $\mathbf{x}$, and $\xi$ are the isoparametric coordinates of point $\mathbf{x}$. This description works satisfactorily as long as displacements are small and concrete has not cracked. When, concrete is highly fragmented and big cracks develop, the linear deformation pattern within a tetrahedral element is no longer meaningful. A more general description for the material point motion is to consider the cells resulting from the Voronoi tessellation (see fig. 1). Each cell is associated to the discrete particle it contains and is limited by triangular facets over which concrete constitutive equations are imposed. In the initial unstressed configuration, all LDPM cells fill the entire volume $V$. Again, each concrete material point is either inside a cell or may be shared with other cells if it is on the external surface of the cell. The motion of a point $\mathbf{x}$ inside a cell can be expressed in terms of velocities as

$$\mathbf{v}(\mathbf{x}, t) = \mathbf{v}_P(t) + \boldsymbol{\omega}_P(t) \times (\mathbf{x} - \mathbf{x}_P) \tag{3}$$

where $\mathbf{x}_P$ is the position of the discrete particle at the center of the cell, $\mathbf{v}_P(t)$ and $\boldsymbol{\omega}_P(t)$ are its velocity and rotation rate vectors. This condition implies that all points inside a cell move rigidly with the cell. While this description may not account for the small deformations that occur in the elasto-plastic range it does a better job in describing the formation of concrete fragments in the post-failure regime and tracking their subsequent motion.

The motion of all material points inside rebars can be described as functions of the velocity and rotation rates of the points along the centerline. The velocity history on an arbitrary point $\mathbf{x}_r$ inside the rebar can be expressed as

$$\mathbf{v}(\mathbf{x}_r, t) = \mathbf{v}(\mathbf{x}_R, t) + \boldsymbol{\omega}(\mathbf{x}_R, t) \times (\mathbf{x}_r - \mathbf{x}_R) \tag{4}$$

where $\mathbf{x}_R$ is the projection of $\mathbf{x}_r$ on the axis of the rebar, and $\mathbf{v}(\mathbf{x}_R, t)$ and $\boldsymbol{\omega}(\mathbf{x}_R, t)$ are the velocity and rotation rate histories of $\mathbf{x}_R$. The displacement history is obtained by integrating the velocity in time

$$\mathbf{u}(\mathbf{x}_r, t) = \int_0^t \mathbf{v}(\mathbf{x}_r, \tau)\, d\tau \tag{5}$$

For each material point inside the rebar or on its interface, there is a corresponding material point inside the concrete. The relative displacement $\mathbf{u}$ and relative velocity $\mathbf{v}$ functions are defined as:

$$\begin{aligned} \mathbf{u}(\mathbf{x}, t) &= \mathbf{u}_c(\mathbf{x}, t) - \mathbf{u}_r(\mathbf{x}, t), \\ \mathbf{v}(\mathbf{x}, t) &= \mathbf{v}_c(\mathbf{x}, t) - \mathbf{v}_r(\mathbf{x}, t) \end{aligned} \tag{6}$$

where the subscript $c$ and $r$ denote concrete and rebar points. Figure 2 shows a schematic representation of a rebar (in red) and the surrounding LDPM tetrahedron (a 2D representative triangle is shown) with the concrete point denoted by c (blue dot) and the rebar point denoted by r (red dot) with both axial and radial springs representing the constraints. For simplicity, constraints are imposed along the axis of the rebar (neglecting the rebar diameter effect) as will be described next.

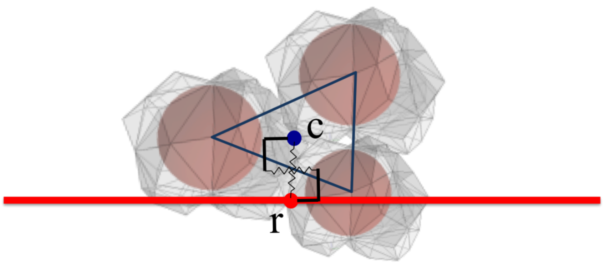


Figure 2: Rebar connected to an LDPM tetrahedron using springs.

### 2.4 Line Constraint Formulation

In its simplest form, we postulate that the internal elastic energy associated to the constraints along the rebar axis can be expressed as a bilinear positive definite symmetric operator $a(\mathbf{u}, \mathbf{u})$ defined as

$$a(\mathbf{u}, \mathbf{u}) = \frac{1}{2} \int_S K\, \mathbf{u} \cdot \mathbf{u}\, ds \tag{7}$$

where $K$ is a stiffness parameter representative of the local compliance of concrete at the rebar interface. The total work performed by the interactive forces $\mathbf{g}$ (force per unit rebar length) is expressed by the linear operator $b(\mathbf{u})$ defined as

$$b(\mathbf{u}) = \int_S \mathbf{g} \cdot \mathbf{u}\, ds \tag{8}$$

For equilibrium, $a(\mathbf{u}, \mathbf{u}) + b(\mathbf{u})$ must be 0. For an arbitrary virtual displacement function $\delta\mathbf{u}$, we obtain

$$\begin{aligned} \delta a + \delta b &= a(\delta\mathbf{u}, \mathbf{u}) + a(\mathbf{u}, \delta\mathbf{u}) + b(\delta\mathbf{u}) \\ &= \int_S K\, \mathbf{u} \cdot \delta\mathbf{u}\, ds + \int_S \mathbf{g} \cdot \delta\mathbf{u}\, ds \\ &= \int_S (K\, \mathbf{u} + \mathbf{g}) \cdot \delta\mathbf{u}\, ds \end{aligned} \tag{9}$$

Since the expression above must be valid for an arbitrary displacement function $\delta\mathbf{u}$, then we have

$$\mathbf{g} = -K\mathbf{u} \quad \text{for each} \quad \mathbf{x} \in S \tag{10}$$

For computational purposes, this expression can be discretized by subdividing the rebar into finite segments and by placing control points at the midpoint of each segment. For a segment of length $\Delta s$ we then have $\mathbf{f} = K\, \Delta s\, \mathbf{u}(\mathbf{x})$

This formulation can be extended to treat non linear condition by using hypo elastic constitutive equation

$$\dot{\mathbf{f}}(t) = \phi(\mathbf{u})\mathbf{v}(t) \tag{11}$$

## 3 NUMERICAL SIMULATIONS

In this section, three beam groups from Ref. [3] are simulated. The groups represent 1D (Group I), 3D (Group II) and 2D (Group III) similarities. The beam dimensions and main reinforcement are listed in Table 1 and a schematic drawing of the beam with supports and loading platens is shown in Fig.3.

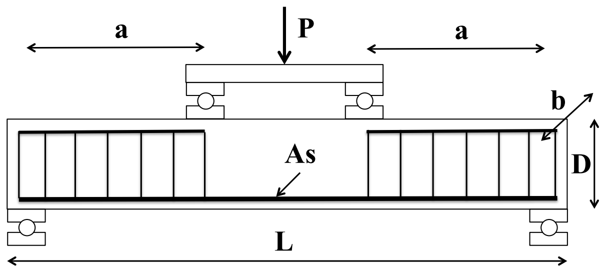


**Figure 3**: Beam dimensions, loading and supports

Only, the 28 days compressive strength $f'_c$ ranging from 17.2 MPa to 20.7 MPa was reported. The concrete mix proportions by weight reported were 0.6:1:2.2:1.8 of water:cement:sand:gravel with max gravel size of 10 mm and maximum sand size of 7 mm. The yield strength was 530 MPa for deformed steel rebars and 220 MPa for plain rebars used as stirrups. No data about the steel modulus of elasticity were available so it was assumed to be 200 GPa.

**Table 1**: Beam Groups Data

| Beam | L × b × h [mm] | a [mm] | As [mm$^2$] |
|---|---|---|---|
| Group I | | | |
| L11×15 | 4600×110×150 | 1960 | 400 |
| L11×30 | 4600×110×300 | 1960 | 800 |
| L11×60 | 4600×110×600 | 1900 | 1600 |
| Group II | | | |
| S5×7 | 1150×55×75 | 480 | 100 |
| M11×15 | 2300×110×150 | 960 | 400 |
| L22×30 | 4600×220×300 | 1900 | 1600 |
| Group III | | | |
| S11×15 | 1150×110×150 | 460 | 400 |
| M11×30 | 2300×110×300 | 930 | 800 |
| L11×60 | 4600×110×600 | 1900 | 1600 |

The following subsections cover the calibration and simulation of model parameters and the analysis of results

### 3.1 Model Calibration

The models used contain two sets of material parameters that need to be identified from experimental data. The first set consists of the LDPM parameters and the second is the penalty stiffness parameter used to provide rebar-concrete interaction.

The calibrated and assumed LDPM parameters for these properties were based on calibrating just for the average compressive strength $f'_c = 18.95$ MPa. With such limited amount of data, and to reduce the degree of redundancy, additional characteristics of concrete were estimated based on literature. The meso-scale tensile strength $\sigma_t$ was set to be equal to the ACI 318-16 splitting strength $f_{sp} = 0.56\sqrt{f'_c} = \sqrt{18.95} = 2.4378$ MPa as was shown in [13]. The Elastic Modulus was computed using the ACI 318-16 relation as $E = 4700\sqrt{f'_c} = 4700\sqrt{18.95} = 20,456$ MPa, then the meso-scale elastic modulus $E_0$ was computed using [12] assuming the poisson's ratio to be 0.176, which gives $\alpha = 0.25$ and $E_0 = 1.5455E = 31,620$ MPa. The initial fracture energy was estimated using [23] as $G_f = (f'_c/0.051)^{0.46}(1 + d_a/11.27)^{0.22}(w/c)^{-0.30} = 20.39$ N/m where $f'_c$ is in MPa, $d_a$ is the maximum aggregate size in mm and $w/c$ is the water to cement ratio by weight. According to [24], the meso-scale fracture energy $G_t$ was found to be equal to the initial fracture energy $G_f$. From the definition of $G_t$ in [12], the meso-scale tensile characteristic length was computed as $l_t = 2E_0G_t/\sigma_t^2 = 217$ mm. Finally, the automatic parameter identification procedure described in [21] was used to identify the shear strength ratio $\sigma_s/\sigma_t$ to match the experimental average $f'_c$ using 3 different geometric realizations of 300×150 mm cylinders. The identification yielded $\sigma_s/\sigma_t = 1.8$. These mentioned parameters are the relevant LDPM parameters needed to describe the unconfined compressive and tensile behavior of concrete as was previously shown in [25]. The remaining parameters were reasonably assumed based on [13]. With these parameters, the average of the simulated concrete compressive strength $f'_{c,num} = 18.89$ MPa, which matches the given experimental data average with an error smaller than 0.3%.

To calibrate the rebar-concrete interaction penalty stiffness $K$ parameter, one can choose a constant value for it or relate it to the properties of the two connected parts. If the first option is utilized then the stiffness value must be large enough to guarantee efficient gluing of rebar segments to the surrounding concrete mesh. This will result in the choice of a very large value that may control the simulation minimum time step as the procedure is explicit. The other option is utilized here where, a segment of the rebar is to be connected to an LDPM tetrahedron. To make the simulation minimum time step independent of the penalty algorithm used, the stiffness $K$ of each constraint is defined as $K = m/\Delta t_p^2$ where $m$ is the minimum nodal mass connected to it ( the rebar node and four LDPM tetrahedron nodes) and $\Delta t_p$ is a selected penalty time step that is always selected to be slightly larger than the simulation minimum time step. Throughout the following, $\Delta t_p$ was always chosen equal to the simulation time step and then a check is done by comparing part of the elastic response of the simulated beam with $\Delta t_p = 2\Delta t$ and $\Delta t_p = 0.1\Delta t$ to make sure that the effect on stiffness is negligible.

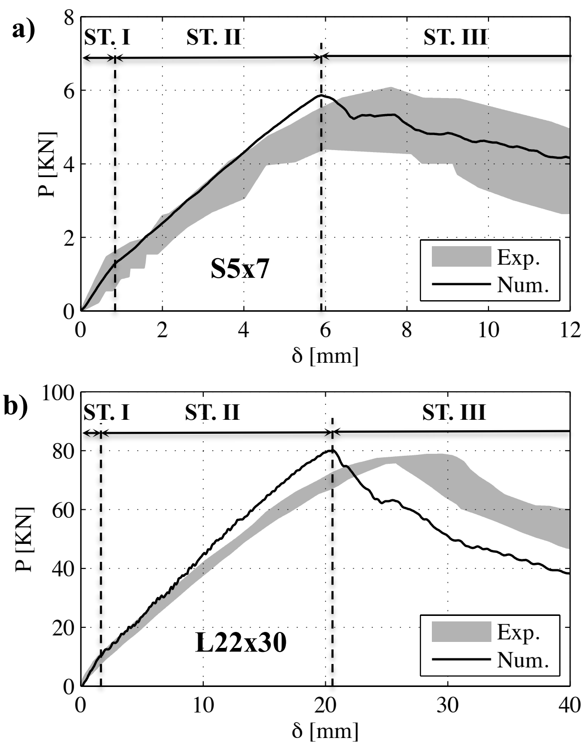


Figure 4: Experimental range and Numerical averages of Load Vs mid-span deflection for beams a) S5×7, and b) L22×30

## 3.2 Simulation Results

The results will be discussed based on three aspects.

First, the load-displacement response. All simulations followed nicely the experimentally reported total load $P_u$ Vs mid span deflection $\delta$ as shown for beams S5×7 and L22×30 in Fig. 4 a&b. The two largely different beam sizes showed three stages of failure, elastic (Stage I), reduced stiffness due to concrete pre-peak cracking (Stage II) and strain softening failure due to concrete post-peak crushing (Stage III). It must be mentioned here that the small differences between simulations and largely scattered experimental clouds are due to the very limited information about the experimental characteristics of concrete and the large range of concrete strength reported for which, the numerical simulations are capturing perfectly the different stages of response.

Second, RC beam load transfer mechanisms at different stages. As shown in Fig.5, crack openings and rebar forces are colored from blue (minimum) to red (maximum). In stage II (Fig.5 a), distributed tensile cracking starts to show around stirrups and mid-span with limited extent over the midspan height due to the large compression zone above it. With the model capability to capture 3D interactions of concrete and the rebars, the stirrups at cracked sections clearly carried higher forces although based on theoretical beam analysis using truss analogy, all stirrups along the shear span should carry the same force. This shows the advantages of this model in capturing local features of the concrete behavior. In stage III (Fig.5 b), the beam midspan crushes clearly with two inclined failure lines, which matches exactly the failure pictures of tested beams in [3]. Finally, the arch action mechanism is clearly shown in Fig.5 c during stage II before concrete crushing. It shows the maximum compressive principal stresses (in blue) which draw an arch between the supports and the mid-span showing the interruptions from distributed cracking in the bottom half of the beam.

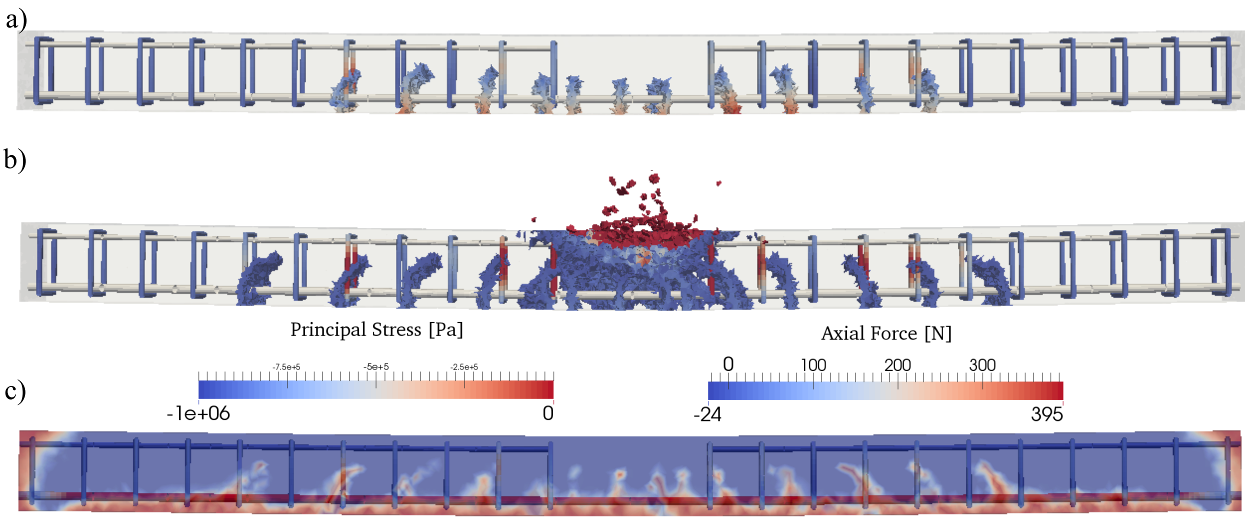


Figure 5: Experimental range and Numerical averages of Load Vs mid-span deflection for beams a) S5×7, and b) L22×30

Third, size effect capturing. Following the same procedure used in [3]. Size effect is represented as a function of a characteristic length and a nominal strength measure based on Bažant's universal size effect law as,

$$\mu = \mu_0 \left(1 + \frac{D}{D_0}\right)^{-1/2} \tag{12}$$

Where $\mu_0 = Bf_t$, $D$ is the chosen characteristic length for comparison, $f_t$ is the direct tensile strength of concrete, $\mu$ is the value of nominal stress corresponding to the ultimate load at the extreme fiber of the beam and both $B$ and $D_0$ are two parameters that depepnd on the structure shape and loading to be identified using regression analysis.

To start the analysis, all elements of Eq. 12 need to be defined. Beam dimensions are shown in Fig. 3. The nominal stress is given by $\mu = 3P_u a/bd^2$ where $P_u$ is the total beam peak load, $a$ is the shear span, $b$ is the beam width and $d$ is the depth to the centroid of main reinforcement. In this paper, the chosen characteristic length for the three groups was the beam total depth $D$. Since no data was given for the tensile strength of the concrete used, $f_t$ was estimated based on concrete compressive strength as $f_t = 0.35\sqrt{f'_c}$ (in MPa) [26].

**Table 2**: Beam Groups Data

| Group | Beam | $P_u$ [KN] Exp. | $P_u$ [KN] Num. | $\mu$ [MPa] Exp. | $\mu$ [MPa] Num. |
|---|---|---|---|---|---|
| I | L11.15a | 13.05 | 11.06 | 46.86 | 39.72 |
| | L11.15b | 13.21 | 10.92 | 47.45 | 39.2 |
| | L11.15c | 10.81 | 10.86 | 38.81 | 39 |
| | L11.30a | 51.92 | 39.27 | 46.62 | 35.26 |
| | L11.30b | 48.75 | 38.33 | 43.77 | 34.42 |
| | L11.30c | 51.62 | 39.48 | 46.35 | 35.45 |
| | L11.60a | 150.54 | 143.34 | 32.76 | 31.19 |
| | L11.60b | 168.22 | 141.21 | 36.6 | 30.73 |
| | L11.60c | 158.47 | 142.76 | 34.48 | 31.06 |
| II | S5.7a | 4.9 | 6.06 | 34.51 | 42.64 |
| | S5.7b | 6.06 | 6.24 | 42.67 | 43.91 |
| | S5.7c | 5.75 | 6.04 | 40.49 | 42.51 |
| | M11.15a | 21.66 | 22.39 | 38.1 | 39.38 |
| | M11.15b | 23.45 | 22.72 | 41.24 | 39.96 |
| | M11.15c | 23.28 | 22.62 | 40.96 | 39.79 |
| | L22.30a | 85.39 | 85.12 | 37.16 | 37.04 |
| | L22.30b | 83.8 | 86.15 | 36.47 | 37.49 |
| | L22.30c | 83.53 | 86.26 | 36.35 | 37.54 |
| III | S11.15a | 62.51 | 65.57 | 52.69 | 55.26 |
| | S11.15b | 39.08 | 66.69 | 32.94 | 56.21 |
| | S11.15c | 56.95 | 64.28 | 48 | 54.18 |
| | M11.30a | 101.73 | 92.7 | 43.34 | 39.49 |
| | M11.30b | 106.58 | 91.79 | 45.41 | 39.11 |
| | M11.30c | 97.34 | 92.59 | 41.47 | 39.44 |
| | L11.60a | 150.54 | 143.34 | 32.76 | 31.19 |
| | L11.60b | 168.22 | 141.21 | 36.6 | 30.73 |
| | L11.60c | 158.47 | 142.76 | 34.48 | 31.06 |

The raw data used for the analysis are listed in Table 2 including for each group, the experimental and numerically simulated peak loads and nominal stresses. To perform the regression analysis, The size effect law is written in a straight line equation form as

$$\begin{aligned} \left(\frac{f_t}{\mu}\right)^{1/2} &= \frac{1}{D_0 B^2} d + \frac{1}{B^2} \\ Y &= Ad + C \end{aligned} \tag{13}$$

So, by using regression analysis, one can compute the two constants $A$ and $C$ in Eq. 13 and then compute back the two size effect law parameters as $D_0 = C/A$ and $\mu_0 = f_t/\sqrt{C}$. As can be seen from Table 2, the experimental data had a large scatter in many cases and it was only limited to 3 beams per each size, while the scatter in numerical simulations was much smaller. For this reason, the Robust Regression method was used, which reduces the effects of outliers using iteratively reweighed Least-Squares Method [27].

The results from regression are used to compute $\mu_0$ and $D_0$ for both experimental and numerical data and are listed in Table 3. Finally, Fig. 6 shows the size effect curve along with the two asymptotes of strength criterion (Horizontal line) and Linear Elastic Fracture Mechanics LEFM (Slope of 2:1) with both experimental and numerical data points for each group. Again, due to the large scatter in experimental data, the values of SEL parameters are different for the experimental vs numerical data for each group but both show clear size effect.

**Table 3**: Size Effect Law Parameters

| Group | $\mu_0$ [MPa] | | $D_0$ [mm] | |
|---|---|---|---|---|
| | Exp. | Num. | Exp. | Num. |
| I | 55.6 | 43.4 | 324 | 501 |
| II | 44.1 | 44.6 | 540 | 553 |
| III | 80.8 | 87.7 | 97 | 68 |

More over, the numerical simulations perfectly align with the SEL curve in all three cases. LDPM simulations were able to capture also the effects of different dimensional similarity on $D_0$ where for 3D Similarity, the results were on the strength theory side (Group II), for 2D similarity, the results were shifted towards the LEFM side (Group III) and 1D similarity was closer to the transitional zone.

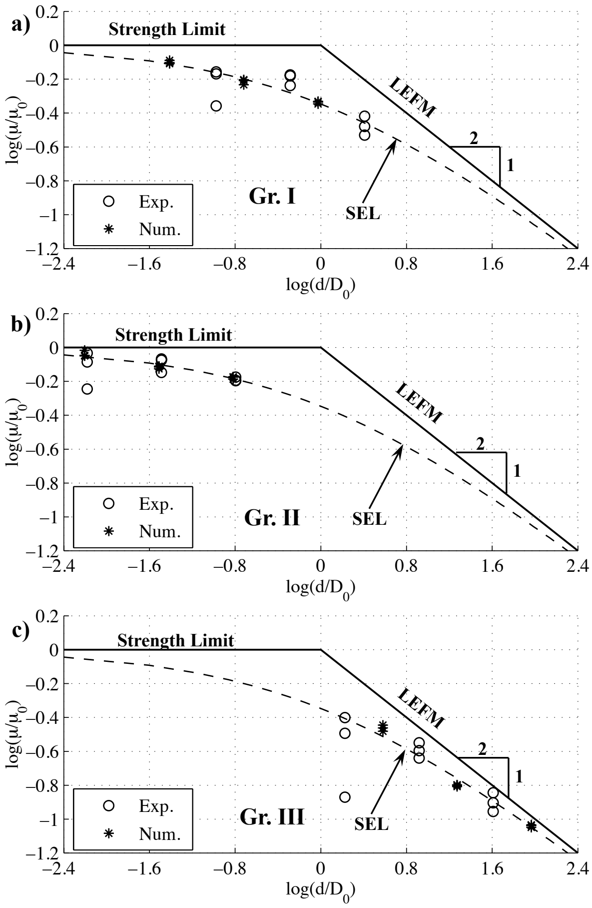


Figure 6: Size Effect Law plots along with strength and LEFM limits for both experimental and numerically simulated values of groups a) I, b) II and c) III

## 4 AKNOWLEDGMENTS

The authors would like to acknowledge the support from the Northwestern University computational center (QUEST) and the Rensselaer Polytechnic Institute Center for Computational Innovations (CCI) to run the simulations in this paper using the High performance computing clusters at both centers. The work of the last author was partially supported by the National Science Foundation under Grant no. CMMI-1435923.

## 5 CONCLUSIONS

In this paper, the Lattice Discrete Particle Model (LDPM) was used to simulate flexural failure of over-reinforced concrete beams of 8 different sizes in 4 point bending loading. The model was able to capture the behavior both qualitatively by replicating as experimental crack pattern and failure mode, and also quantitively by replicating the load displacement responses and peak load values. Most notably, the model was able to capture size effects in the three different groups with 1D, 2D and 3D geometric similarities which - to the knowledge of the authors - is the first time, a concrete model replicates such size effects in over-reinforced beams failure. Additionally, the model was able to capture general aspects of beam behavior and load transfer mechanisms over different stages of loading including elastic, pre-peak crack initiation and post-peak damage and crushing of concrete. It was also able to show how concrete and steel (both longitudinal and vertical) reinforcement exchange forces around cracked areas along the beam.

## REFERENCES


[1] Z. P. Bažant and Y. W. Kwon. *Failure of slender and stocky reinforced concrete columns: tests of size effect*, volume 27.

[2] S. L. Burtscher and J. Kolleger. *Size effect experiments on granular materials in compression*. In L. et. al. (EDs.), Fracture Mechanics of Concrete Structures, IA-FraMCos, 2004.

[3] C. M. Belgin and S. Sener. Size effect on failure of overreinforced concrete beams. *Engineering Fracture Mechanics*, 75:2308–2319, 2008.

[4] Z. P. Bazant and J. Planas. *Fracture and Size effect in concrete and other quasibrittle materials*. CRC Press LLC, 1998.

[5] Zdenek P. Bazant and Drahomir Novak. Energetic-statistical size effect in quasibrittle failure at crack initiation. *Materials Journal*, 97(3), 2000.

[6] Size effect in blunt fracture: Concrete, rock, metal. *Journal of Engineering Mechanics*, 110(4):518–535, 1984.

[7] Compression failure of beams made of different concrete types and sizes. *Journal of Structural Engineering*, 126(2):200–209, 2000.

[8] J. G. M. van Mier and J. P. Ulfkjær. Round-robin analysis of over-reinforced concrete beams—comparison of results. *Materials and Structures*, 33(6):381–390.

[9] G. Cusatis and Z.P. Bažant. Size effect on compression fracture of concrete with or without v-notches: a numerical meso-mechanical study. *Computational Moedelling of Concrete Structures-Meschke,de Borst, Mang & Bicanic (eds), Taylor & Francis Group, London*, 2006.

[10] P. Droz and Z.P. Bažant. Nonlocal analysis of stable states and stable paths of propagation of damage shear bandd. in cracking and damage, strain localization and size effect. *J. Mazars and Z.P. Bazant, eds, Elsevier Applied Science, London*, pages 183–207, 1989.

[11] Compression failure of quasibrittle material: Nonlocal microplane model. *Journal of Engineering Mechanics*, 118(3):540–556, 1992.

[12] G. Cusatis, D. Pelessone, and A. Mencarelli. Lattice discrete particle model (ldpm) for concrete failure behavior of concrete. i: Theory. *Cement and Concrete Composites*, 33(9):881–890, 2011.

[13] G. Cusatis, A. Mencarelli, D. Pelessone, and J.T. Baylot. Lattice discrete particle model (ldpm) for failure behavior of concrete. ii: Calibration and validation. *Cement and Concrete Composites*, 33(9):891–905, 2011.

[14] G. Cusatis and E.A. Schauffert. Discontinuous cell method (dcm) for cohesive fracture propagation. In *Proceedings of the 7th international conference on fracture mechanics of concrete and concrete structures (FraMCos 7)*, pages 23–28, (Jeju, South Korea), Korea Concrete Institute, 2010.

[15] R. Rezakhani and G. Cusatis. Generalized mathematical homogenization of the lattice discrete particle model. In *Proceedings of the 8th International Conference on Fracture Mechanics of Concrete and Concrete Structures, FraMCoS 2013*, pages 261–271, Toledo, Spain, 2013.

[16] G. Cusatis and X. Zhou. High-order microplane theory for quasi-brittle materials with multiple characteristic lengths. *Journal of Engineering Mechanics*, 140(7):04014046, 2014.

[17] Ed A. Schauffert and Gianluca Cusatis. Lattice discrete particle model for fiber reinforced concrete (ldpm-f): I. theory. *Journal of Engineering Mechanics*, 138(7):826–833, 138.

[18] Ed A. Schauffert, Gianluca Cusatis, D. Pelessone, J.L. O'Daniel, and J.T. Baylot. Lattice discrete particle model for fiber reinforced concrete (ldpm-f): Ii. tensile fracture and multiaxial loading behavior. *Journal of Engineering Mechanics*, 138(7):834–841, 138.

[19] Jovanca Smith, Gianluca Cusatis, Daniele Pelessone, Eric Landis, James O'Daniel, and James Baylot. Discrete modeling of ultra-high-performance concrete with application to projectile penetration. *International Journal of Impact Engineering*, 65:13–32, 2014.

[20] Roozbeh Rezakhani and Gianluca Cusatis. Asymptotic expansion homogenization of discrete fine-scale models with rotational degrees of freedom for the simulation of quasi-brittle materials. *Journal of the Mechanics and Physics of Solids*, 88:320 – 345, 2016.

[21] Mohammed Alnaggar and Gianluca Cusatis. Automatic parameter identification of discrete mesoscale models with application to the coarse-grained simulation of reinforced concrete structures. *20th Analysis and Computation Specialty Conference*, 36:406–417, 2012.

[22] G Cusatis, R Rezakhani, M Alnaggar, X Zhou, and D Pelessone. *Multiscale computational models for the simulation of concrete materials and structures*, pages 23–38. CRC Press, 2015/02/26 2014.

[23] Statistical prediction of fracture parameters of concrete and implications for choice of testing standard. *Cement and Concrete Research*, 32(4):529 – 556, 2002.

[24] Two-scale study of concrete fracturing behavior. *Engineering Fracture Mechanics*, 74(12):3 – 17, 2007. Fracture of Concrete Materials and Structures.

[25] Mohammed Alnaggar. *Multiscale Modeling of Aging and Deterioration of Reinforced Concrete Structures*. PhD thesis, NORTHWESTERN UNIVERSITY, 2014.

[26] Ts500 turkish standards, requirements for design and construction of reinforced concrete structures, ankara, turkey 2003.

[27] Paul W. Holland and Roy E. Welsch. Robust regression using iteratively reweighted least-squares. *Communications in Statistics - Theory and Methods*, 6(9):813–827, 1977.